In-situ Synthesis and Unprecedented Electrochemical Performance of Double Carbon Coated Cross-linked Co_3O_4

Ying Wang,[1] Shijia Fan,[1] Shengxiang Wu,[1] Chao Wang,[1] Zhenguo Huang,*[2] Lei Zhang*[3]*

[1]School of Chemistry & Materials Science, Jiangsu Key Laboratory of Green Synthetic Chemistry for Functional Materials, Jiangsu Normal University, Xuzhou, Jiangsu 221116, China.

[2]School of Civil & Environmental Engineering, University of Technology Sydney, NSW 2007 Australia.

[3]Centre for Clean Environment and Energy, Griffith University, Queensland 4222, Australia.

KEYWORDS: Lithium ion battery, transition metal oxides, double carbon coating, Co_3O_4, electrochemical performance.

ABSTRACT

Improving the structural stability and the electron/ion diffusion rate across whole electrode particles is crucial for transition metal oxides as next-generation anodic materials in lithium ion batteries. Herein, we report a novel structure of double carbon coated Co_3O_4 cross-linked composite, where Co_3O_4 nanoparticle is *in-situ* covered by nitrogen-doped carbon and further connected by carbon nanotubes (Co_3O_4 NP@NC@CNTs). This double carbon coated Co_3O_4 NP@NC@CNTs framework not only endows a porous structure that can effectively accommodate the volume changes of Co_3O_4, but also provides multidimensional pathways for electronic/ionic diffusion in and among the Co_3O_4 nanoparticles. As expected, the Co_3O_4 NP@NC@CNTs electrode exhibits unprecedented lithium storage performance, with high reversible capacity of 1017 mAh g^{-1} after 500 cycles at 1 A g^{-1}, and very good capacity retention of 75%, even after 5000 cycles at 15 A g^{-1}. The lithiation/delithiation process of Co_3O_4 NP@NC@CNTs is dominated by pesudocapacitive behavior, resulting in excellent rate performance and durable cycle stabiltiy. Electrochemical kinetics further reveals a decreased energy barrier for electron/ion transport, synergistically, contributes to its excellent lithium storage performance.

1. Introduction

Transition metal oxides (TMOs, M = Zn, Co, Fe, Ni, *etc.*) have received intense interest as potential anodic materials for lithium ion batteries (LIBs), owing to their high theoretical capacity and natural abundance.[1-5] The practical applications of TMOs, however, are hindered by the following reasons. a) Severe volume changes (e.g. ~100 % for Co_3O_4) during the Li^+ insertion/extraction cycles, resulting in electrode pulverization and finally peeling off from the current collector, leading to irreversible capacity loss. b) Poor rate performance that is based in the nature of TMOs

and their discharge mixture (TM/Li_2O). To date, various efforts have been devoted to address the above issues.[6-10] In particular, embedding TMOs into carbon matrix has attracted enormous interest.[12-15] For example, Yang *et al.* reported excellent electrochemical performance of their ZnO nanoparticles (NPs)@nitrogen-doped carbon (NC) hybrids[1]. Our group reported the superior sodium storage performance of zeolitic imidazolate framework-67 (ZIF-67) derived Co_3O_4 NP@NC hybrid.[16] Although great achievements have been obtained, a key disadvantage of these single carbon/TMOs is their limited interfacial conductivity and connectivity between individual carbon/TMO particles, which results in relatively low utilization of the TMO NPs.[17,18] It is, therefore, crucial to introduce an "intermediary" to reinforce the conductive contact between different electrode particles.{Liu, 2015 #3317;Guo, 2015 #3321;Wang, 2016 #3344}. However, the investigation about such dual carbon coated electrode is still in its infancy.

Carbon nanotubes (CNTs), which exhibit great mechanical strength and excellent electrical conductivity, are an ideal candidate to act as intermediary.{Wu, 2013 #3320} Electrodes with CNTs such as Fe_3C@N–CNTs,[19] ZnO@NC@CNTs hybrids,[20] and NiP_2@C-CNTs,[21] have shown enhanced electrochemical performance. Recently, Chen *et al.* reported an *in-situ* synthesized "sea urchin" like Co NPs@CNTs framework by using ZnCo-MOFs as precursor, and confirmed that the interconnected CNTs could facilitate both local and interfacial electron transportation in the electrode.[22] To date, many works have focused on the TMO NPs@carbon or TMO NPs@CNTs hybrids, however, the structural superiority of TMO NPs@carbon@CNTs formed *in-situ* has been ignored.

Inspired by the above considerations and the feasibility of growing CNTs *in-situ* by a proper pyrolysis process, herein, we designed a novel structure that connected the Co_3O_4 NPs@NC units *in-situ* by CNTs. Through a pyrolysis-oxidation strategy a simple ZIF-67 precursor was converted

to Co_3O_4 NPs (3−7 nm) that were covered by NC layers, and further connected by intertwined CNTs, forming a unique double carbon coated Co_3O_4 NP@NC@CNTs framework. On the one hand, the ultra-small Co_3O_4 NP@NC units effectively shorten the electronic/ionic diffusion distances and alleviate the electronic/ionic conductivity of a single unit. On the other hand, the interconnected CNTs enhance the conductive contact between different Co_3O_4 NP@NC units. In addition, the porous structure of the Co_3O_4 NP@NC@CNTs can effectively accommodate the volume changes and facilitate better contact between the electrolyte and the electrode. Therefore, unprecedented electrochemical performance is observed in the Co_3O_4 NP@NC@CNTs based electrode, which shows high reversible capacity, excellent rate capability, and extraordinary cycling stability under super-high current densities. In particular, high capacities of 1017 and 235 mAh g^{-1} are delivered at 1.0 and 15 A g^{-1} after 500 and 5000 cycles, respectively. To the best of our knowledge, such outstanding electrochemical performance had been rarely reported for Co_3O_4-based anodic materials in LIBs. Although metal-organic frameworks (MOFs) have been used as precursors to obtain TMO NPs@carbon hybrids,[12-15] further improvement to synthesis such double carbon coated TMOs is still in its infancy due to the limited reports on this research field. Therefore, our work may shed light on novel designs for other TMO-based electrodes with high electrochemical performance.

2. Experimental Section

2.1 Synthesis of Co_3O_4 NP@NC@CNTs networks: The Co_3O_4 NP@NC@CNTs networks were derived by first converting ZIF-67 into Co NP@NC, followed by annealing under an Ar/C_2H_2 gas mixture (10% C_2H_2), and then oxidizing to Co_3O_4 NP@NC@CNTs. Briefly, the ZIF-67 derived Co NP@NC was synthesized according to our previous report[1]. Then, the Co NP@NC powders

were transferred into a tube furnace and heated to 600 °C (ramp rate: 10 °C min^{-1}), and then held for 30 min under the Ar/C_2H_2 gas mixture. After naturally cooling down to room temperature, the resultant sample was further oxidized at 200 °C for 24 h in air. The target sample is denoted as Co_3O_4 NP@NC@CNTs. ZIF-67 derived Co_3O_4 NP@NC was synthesized by directly oxidized the Co NP@NC, under same conditions as the Co_3O_4 NP@NC@CNTs.

2.2 Structural and physical characterization: X-ray diffraction (XRD, Rigaku D/Max-2500, Cu Kα radiation), field-emission scanning electron microscopy (FESEM, JEOL, SU8010), transmission electron microscopy (TEM), high-resolution TEM (HRTEM, JEOL JEM-2010FEF), thermogravimetric analysis (TGA, TA-Q50), N_2 adsorption/desorption isotherms (Quantachrome, Autosorb-IQ2-VP), X-ray photoelectron spectroscopy (XPS, Thermo ESCALAB 250XI), and Raman spectroscopy (Renishaw inVia, excitation 514.5 nm) were employed for morphological and structural investigations. The electrical conductivity of samples was tested based on a four-probe system (RST-9).

2.3 Electrochemical testing: The electrochemical performance of samples were evaluated by assembling 2032 coin cell batteries. Typically, active materials, conductive carbon black, and polyvinylidene fluoride (PVDF) were mixed in a weight ratio of 8:1:1, dispersed in N-methyl-2-pyrrolidone (NMP), and then milled for 30 min to form a slurry. The slurry was cast onto copper foil using a doctor blade, and vacuum dried at 80 °C overnight. The loading mass of Co_3O_4 NP@NC and Co_3O_4 NP@NC@CNTs is around 0.9 and 0.8 mg cm^{-2}, respectively. Lithium discs (MTI Corporation) were used as the counter electrode. 1 M $LiPF_6$ (Sigma Aldrich) in ethylene carbonate (EC, Sigma Aldrich), diethyl carbonate (DEC, Alfa Aesar), and fluorinated ethylene carbonate (FEC, Sigma Aldrich) (volume ratio 6:3:1) was used as the electrolyte. Polypropylene (PP, MTI Cooperation) was used as the separator. The cells were assembled in an argon-filled

glove box with the oxygen and water content below 0.1 ppm. Galvanostatic charge-discharge tests were carried out at room temperature on a battery testing system (LAND Wuhan, China) in the potential range of 0.01−3.00 V (*vs.* Li/Li$^+$). Cyclic voltammetry (CV) tests and electrochemical impedance spectroscopy (EIS) measurements were performed on a CHI660E electrochemical work station. The specific capacity in this work were calculated based on Co_3O_4 NP@NC or Co_3O_4 NP@NC@CNTs.

3. Results and Discussion

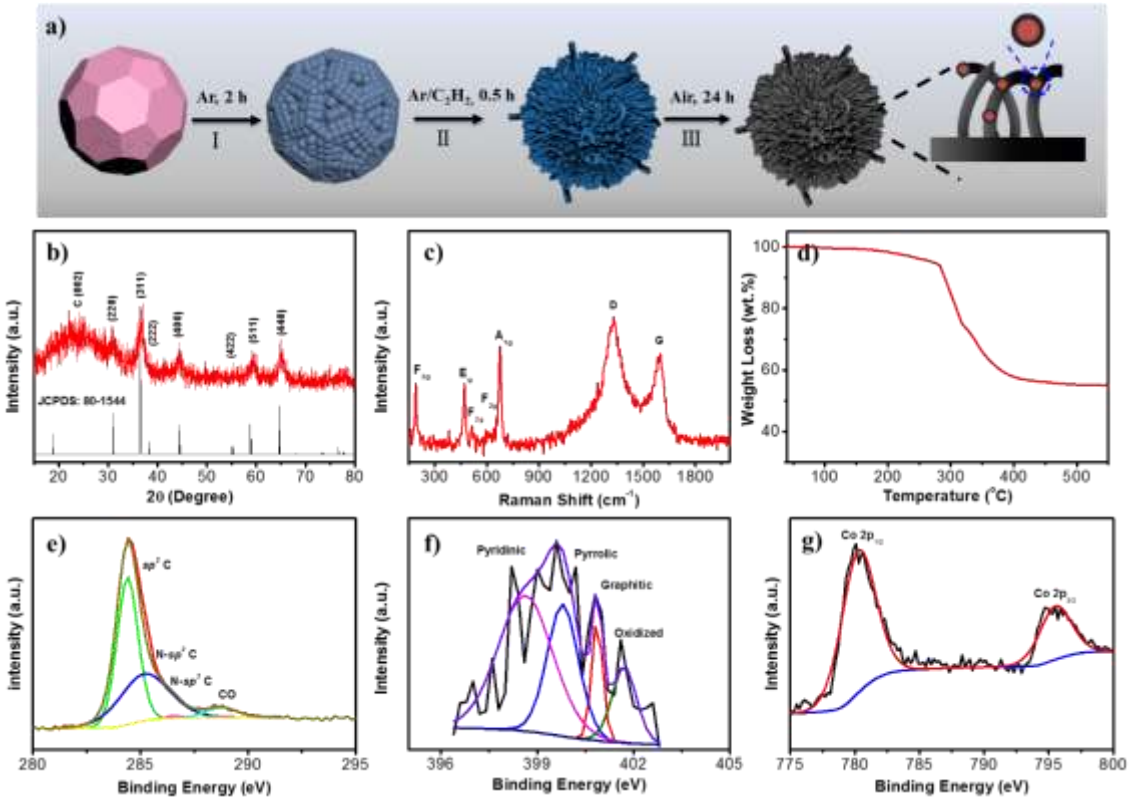

Figure 1. (a) Schematic illustration for the synthesis procedure of Co_3O_4 NP@NC@CNTs framework. (b) XRD pattern, (c) Raman spectrum, (d) TGA curve (in air), and high resolution XPS spectra of (e) C 1s, (f) N 1s, and (g) Co 2p peaks of Co_3O_4 NP@NC@CNTs.

Synthesis procedure for the Co_3O_4 NP@NC@CNTs framework is illustrated in Figure 1a. By pyrolyzing the ZIF-67 precursors in Ar, the surfaces of the polyhedra changed from smooth to rough (Figure S1 in the Supporting information), indicating formation of the Co NP@NC subunits (Figure S2). Subsequently, Co in the Co NP@NC units catalyzed the growth of CNTs under an Ar/C_2H_2 mixture gas. Meanwhile, when annealed the Co NP@NC at 600 °C in Ar for 30 min, no CNTs was observed (Figure S3), further confirming that CNTs in Co_3O_4 NP@NC@CNTs is generated by the decomposition of C_2H_2. After a careful oxidation process in air, the unique Co_3O_4 NP@NC@CNTs framework obtained. The good permeation of Ar/C_2H_2 resulted in homogeneous CNTs growth in the resultant sample (Figure S1e, f). A ZIF-67 derived Co_3O_4 NP@NC framework was also prepared for comparison.

XRD pattern of the Co_3O_4 NP@NC@CNTs framework displays several peaks at 31.0°, 36.6°, 38.2°, 44.4°, 52.2°, 58.8°, and 64.7°, that can be ascribed to the (220), (311), (222), (400), (422), (511), and (440) planes of cubic Co_3O_4 (JCPDS No. 80-1544), respectively (Figure 1b). The broad peak at 23.8° is attributed to the (002) planes of graphitic carbon. Notably, the diffraction peaks of Co_3O_4 are broad and weak, indicating small crystal size. The Raman spectrum was used to acquire more structural information on the Co_3O_4 NP@NC@CNTs framework (Figure 1c). The typical Co_3O_4 mode vibrations F_{2g}, E_g, F_{2g}, F_{2g}, and A_{1g} are observed.[23] Meanwhile, the typical D band (1325 cm^{-1}) for disordered carbon and the G band (1591cm^{-1}) for graphitic carbon are present, in agreement with the co-existence of amorphous NC and CNTs. For the Co_3O_4 NP@NC sample, the D band and G band are located at 1328 and 1594 cm^{-1}, respectively (Figure S3). The slight shift of these bands in Co_3O_4 NP@NC@CNTs indicates good connections between the Co_3O_4 NP@NC units and the CNTs. The TG curve (Figure 1d) indicates a total weight loss of 44 wt.% in air, causes

by evaporation of NC and CNTs in the Co_3O_4 NP@NC@CNTs. The Co_3O_4 NP@NC lost only 26 wt.% under same conditions (Figure S4). Therefore, the Co_3O_4 NP@NC@CNTs is composed of about 18 wt.% CNTs, 26 wt.% NC, and 56 wt.% Co_3O_4 NPs.

The XPS spectra reveal the chemical states of C, N, and Co (Figure 1e−g). The deconvolution of the C 1s spectrum reveals four peaks at 284.6, 285.2, 286.6, and 288.6 eV, corresponding to the sp^2 C-C, sp^2 C-N, sp^3 C-N, and C-O (physical absorption) bonds, respectively.[24,25] The N 1s spectrum has four components centered at 398.9, 400.1, 401.1, and 401.9 eV, representing pyridinic N, pyrrolic N, graphitic N, and oxidation N, respectively.[25-27] Pyridinic and pyrrolic N are dominant in Co_3O_4 NP@NC@CNTs, which is believed to be of benefit for the electrolyte wettability and provide better conductivity.[28,29] The spectrum of Co 2p exhibits two dominant peaks at 780.3 and 795.5 eV, representing the $2p_{1/2}$ and $2p_{3/2}$ peaks of Co_3O_4.[16] The XPS results are in agreement with the XRD patterns and Raman analysis.

TEM images of Co_3O_4 NP@NC@CNTs are shown in Figure 2a and b. The Co_3O_4 NP@NC@CNTs maintains the polyhedral outline of the ZIF-67 precursor and displays a uniform particle size of ~150 nm. Unlike Co_3O_4 NP@NC (Figure S5), abundant CNTs are observed in the Co_3O_4 NP@NC@CNTs (Figure 2a). Figure 2b shows that the outer diameter of the CNTs ranges from 9 to 12 nm, and the Co_3O_4 NP@NC units are wrapped by CNTs. HR-TEM (Figure 2c, d) images better represent the architecture of Co_3O_4 NP@NC@CNTs. The lattice spacing of 0.28 nm at point A corresponds to the (220) planes of cubic Co_3O_4. The short and curved lattice fringes with a d-space of 0.37 nm at point B are associated with the (002) planes of NC. CNTs that covering the Co_3O_4 NP@NC units are marked as C, which show an expanded (002) interplanar space of 0.42 nm, causing by the relative lower formation temperature and/or short annealing time. Small graphitic layers are randomly stacked forming the walls of CNTs, which indicated more defects

and edges in the CNTs. Furthermore, abundant mesopores (point D) can be found inside the Co_3O_4 NP@NC@CNTs framework. Bright spots assigned to Co_3O_4 NPs (about 3−7 nm in diameter) are observed in the high-angle annular dark field mode (HAADF, Figure 2e). The energy dispersive X-ray spectroscopy (EDX, Figure 2f)) spectrum demonstrates the homogeneous distribution of Co, O, C, and N in the framework. The porous nature of Co_3O_4 NP@NC@CNTs was examined by N_2 isotherms (Figure S6a). A type IV hysteresis loop is observed, indicating that the Co_3O_4 NP@NC@CNTs has a mesoporous structure. The specific surface area of Co_3O_4 NP@NC@CNTs is 372 m^2 g^{-1}, larger than the 101 m^2 g^{-1} for Co_3O_4 NP@NC (Figure S6b). The larger surface area of Co_3O_4 NP@NC@CNTs is caused by the intertwined CNTs, which is of benefit for the charge and mass transport in the electrode.

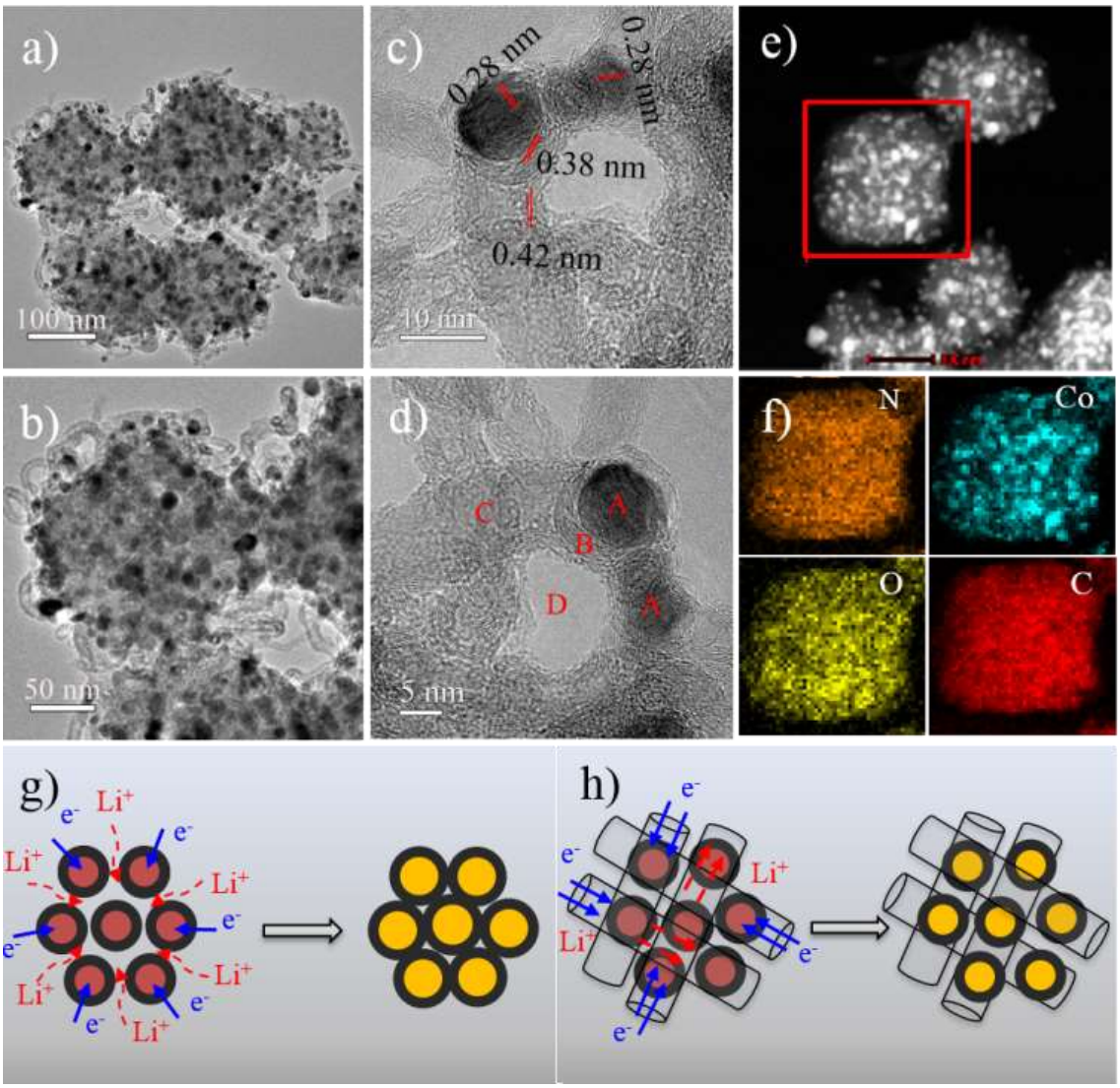

Figure 2. Morphology and architecture characterization of Co_3O_4 NP@NC@CNTs. (a, b) TEM, (c, d) HR-TEM, and (e) HAADF mode images, and (f) EDX elemental mapping of N, Co, O, and C, corresponding to the red square in (e). The scale bar in (e) is 100 nm. (g) and (h) illustrate the lithiation process for the Co_3O_4 NP@NC and Co_3O_4 NP@NC@CNTs frameworks.

Figure 2g, h illustrates the structural superiority of this double carbon coated Co_3O_4 NP@NC@CNTs framework. Although the NC layer in the Co_3O_4 NP@NC sample improves the conductivity of the individual Co_3O_4 NPs, the poor contact between different Co_3O_4 NPs is

unfavorable for electron/Li^+ transport, which results in low utilization of the electrode.[17,18] In the case of Co_3O_4 NP@NC@CNTs, the Co_3O_4 NP@NC units are distributed along the CNTs, forming multidimensional pathways for efficient electron/Li^+ transport. The CNT skeleton can not only provide multidimensional channels for rapid electron/ion transport in/among the Co_3O_4 NP@NC units, but also effectively buffers the stress during volume expansion/shrinkage, resulting in excellent rate ability and cycling stability. In addition, the *in-situ* grown CNTs provide a large contact area between the electrolyte and the electrode.

The electrochemical performance of this novel Co_3O_4 NP@NC@CNTs electrode was investigated, and compared with ZIF-67 derived Co_3O_4 NP@NC. The first lithiation process of Co_3O_4 NP@NC (Figure 3a) results in a small peak at ~1.0 V that is assigned to reduction of Co^{3+} to Co^{2+}, and a dominant peak at ~0.8 V that reflects reduction of Co^{2+} to Co and the formation of a solid electrolyte interphase (SEI) film.[30,31] The anodic peak at ~2.1 V is associated with oxidation of Co to Co^{2+}.[23] During the following cycles, the reduction peak of Co^{2+} shifts to ~1.1 V, which is caused by the dispersion of Co into the Li_2O matrix.[32] The Co_3O_4 NP@NC@CNTs shows similar cathodic and anodic peaks (Figure 3b). The stronger and more stable peaks in Co_3O_4 NP@NC@CNTs suggest higher Li^+ storage and easier electrochemical kinetics.[23] Figure S7 compares the initial four discharge/charge profiles of Co_3O_4 NP@NC@CNTs and Co_3O_4 NP@NC. In the first cycle, Co_3O_4 NP@NC@CNTs delivers a discharge and charge capacity of 1559 and 1011 mAh g^{-1}, respectively, much higher than that of Co_3O_4 NP@NC (1294 and 892 mAh g^{-1} for discharge and charge), confirming better utilization of the Co_3O_4 NP@NC@CNTs electrode. The irreversible capacity loss in the first cycle may be caused by the formation of the SEI film and the irreversible reduction of Co_3O_4.[33,34] In the subsequent cycles, the Coulombic efficiency (CE) reaches ~100%, indicating high stability of the electrode. A significant difference between the discharge/charge

profiles of Co_3O_4 NP@NC@CNTs and Co_3O_4 NP@NC is the capacity contribution below 0.5 V. The Co_3O_4 NP@NC@CNTs shows ~416 mAh g^{-1} in the voltage range of 0.01−0.5V, while Co_3O_4 NP@NC delivers 341 mAh g^{-1}. The extra capacity of Co_3O_4 NP@NC@CNTs in this voltage range is attributed to the contribution of CNTs, which provide more active sites for Li^+ storage.

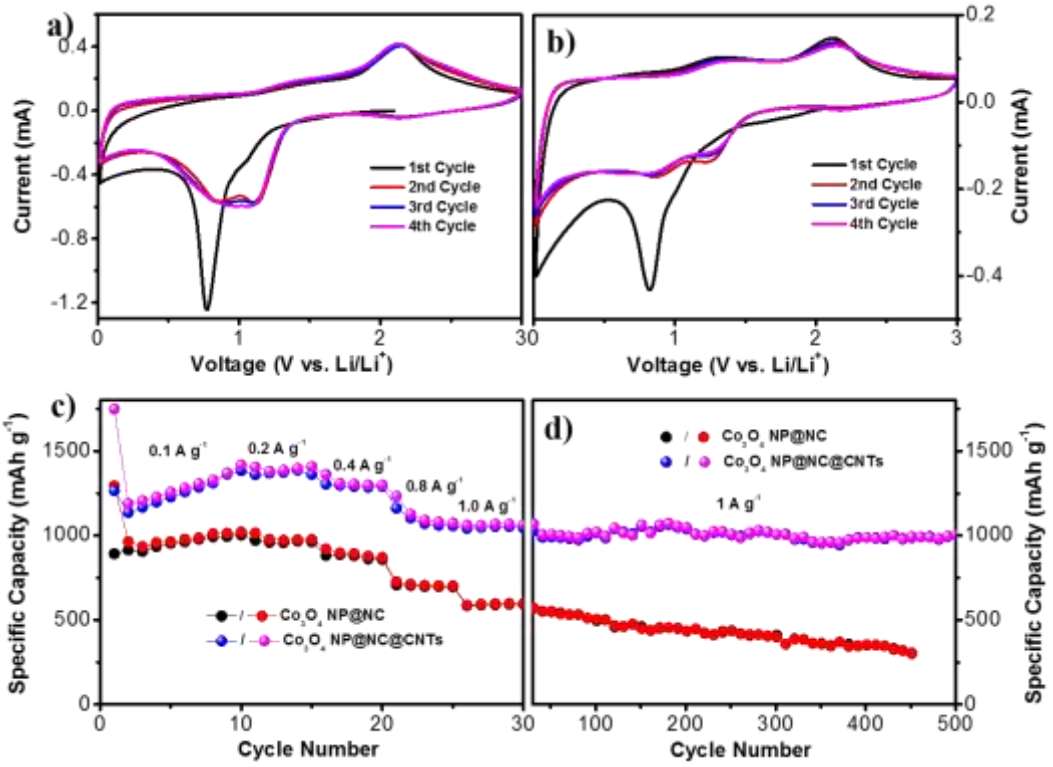

Figure 3. Cyclic voltammetry curves for the initial four cycles of (a) Co_3O_4 NP@NC, and (b) Co_3O_4 NP@NC@CNTs, from 0.01 to 3.0 V *vs.* Li/Li^+. (c) Rate capability of Co_3O_4 NP@NC@CNTs and Co_3O_4 NP@NC at various current densities, from 0.1 to 1 A g^{-1}, and (d) cycling performance of Co_3O_4 NP@NC@CNTs and Co_3O_4 NP@NC at 1.0 A g^{-1} after the rate capability test.

Figure 3c displays the rate performance of Co_3O_4 NP@NC@CNTs and Co_3O_4 NP@NC. During the initial 10 cycles at 0.1 A g^{-1}, the capacity of Co_3O_4 NP@NC@CNTs gradually increases to

1427 mAh g^{-1}, which may be due to continuous activation.[35] The discharge capacity of Co_3O_4 NP@NC@CNTs is maintained at about 1413, 1314, 1100, and 1074 mAh g^{-1} at 0.2, 0.4, 0.8, and 1.0 A g^{-1}, respectively. Although capacity of the Co_3O_4 NP@NC electrode is comparable to that of the Co_3O_4 NP@NC@CNTs at low current, the superiority of the Co_3O_4 NP@NC@CNTs becomes clear at high current. The cycling performance at 1.0 A g^{-1} is presented in Figure 3d. The Co_3O_4 NP@NC@CNTs still delivers 1017 mAh g^{-1} after 500 cycles, demonstrating its excellent capacity retention (95%). The electrochemical performance of Co_3O_4 NP@NC@CNTs is much better than the Co_3O_4 NP@NC and other composites reported in the literature, as shown in Table S1, indicating the structural superiority of the Co_3O_4 NP@NC@CNTs framework.

The amazing electrochemical performance of the Co_3O_4 NP@NC@CNTs electrode inspired further electrochemical investigation at ultrahigh current densities (1.0−15 A g^{-1}, Figure 4a). The Co_3O_4 NP@NC@CNTs is able to deliver high capacities of 989, 924, 758, 618, and 537 mAh g^{-1} at current densities of 1.0, 2.0, 4.0, 6.0, and 8.0 A g^{-1}, respectively. Even at 10 and 15 A g^{-1}, this electrode can still deliver 459 and 321 mAh g^{-1}. Moreover, when the current density returned to 1.0 A g^{-1}, a high reversible capacity of 1140 mAh g^{-1} recovered. Detailed capacity retention of this Co_3O_4 NP@NC@CNTs electrode at various current densities is given in Figure 4b. The long-life cycling performance of Co_3O_4 NP@NC@CNTs at 15 A g^{-1} is presented in Figure 4c. High capacity of 240 mAh g^{-1} is still delivered after 5000 cycles at this super-high current density, corresponding to 75% capacity retention. The excellent structural stability of Co_3O_4 NP@NC@CNTs is further confirmed by its CE, which remains at ~100% during the 5000 cycles (except for the first cycle). The electrochemical performance comparison of this Co_3O_4 NP@NC@CNTs with other highly studied Co-based electrodes in Figure 4d further demonstrates its superiority. The Co_3O_4 NP@NC@CNTs shows 95% capacity retention at 1 A g^{-1} after 500 cycles, and 75% capacity

retention even at 15 A g^{-1} after 5000 cycles, outperforming most other reported results.[33-38]

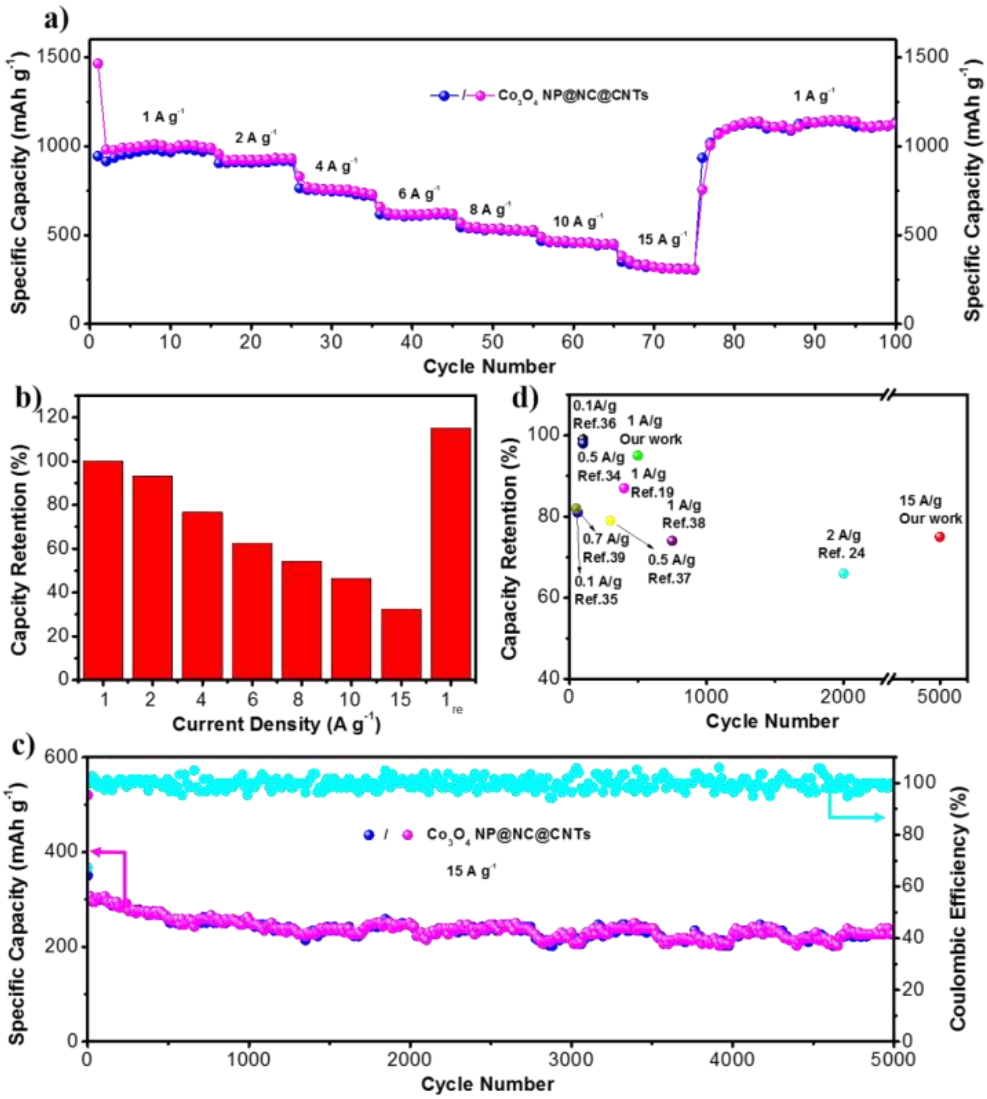

Figure 4. Electrochemical investigation of Co_3O_4 NP@NC@CNTs electrode. (a) High rate performance from 1.0 to 15 A g^{-1}, (b) capacity retention at different current densities, (c) long-life cycling performance at 15 A g^{-1}, (d) comparsion of capacity retention and cycling performance between Co_3O_4 NP@NC@CNTs and other Co-based electrodes.

To understanding the kinetics mechanisms of such excellent electrochemical performance,

electrochemical impedance spectroscopy (EIS) analysis of Co_3O_4 NP@NC and Co_3O_4 NP@NC@CNTs was carried out. As demonstrated in Figure 5a and b, all the Nyquist plots contain a semicircle that is related to the charge transfer resistance (R_{ct}) and a sloping line that is related to the Warburg diffusion process. As the testing temperature is increased to higher values, the R_{ct} decreases to lower values, indicating faster charge transfer kinetics. In addition, the Co_3O_4 NP@NC@CNTs shows a smaller semicircle than that of Co_3O_4 NP@NC (at the same temperature), meaning lower R_{ct} resistance in the electrochemical reactions, which contributes to an easier electrochemical process. The apparent activation energy (E_a) for lithiation of both samples was calculated according to the following Equations: [4]

$$i_0 = RT/nFR_{ct} \quad (1)$$

$$i_o = Aexp(E_a/RT) \quad (2)$$

where i_0 is the exchange current, A is a temperature independent coefficient, R is the ideal gas constant, T is the absolute temperature, n is the number of transferred electrons, and F is the Faraday constant. Figure 5c shows the Arrhenius plots of Co_3O_4 NP@NC and Co_3O_4 NP@NC@CNTs, where E_a equals to the slope of the fitting curve multiplied by R. Detailed data for the Arrhenius fitting is given in Table S2. The E_a is 63.7 kJ mol^{-1} for Co_3O_4 NP@NC and 62.9 kJ mol^{-1} for Co_3O_4 NP@NC@CNTs. The lower E_a value of Co_3O_4 NP@NC@CNTs indicates a more facile lithiation process.

To further investigate the electrochemical kinetics of this novel double carbon coated structure, a CV test was performance at different scan rate. As shown in Figure 5d, all the peak currents (i) increase as the scan rates (v) increase. Generally, the scan rate and the measured current obey following laws, given in Equation 3-4.

$$i = av^b \quad (3)$$

$$logi = b \times logv + loga \quad (4)$$

$$i = k_1 v^{1/2} + k_2 v \quad (5)$$

Herein, *a* and *b* stand for empirical parameters. When *b* is close to 0.5, the electrochemical performance is dominated by a Faradaic process; when b is close to 1.0, the system features pesudocapacitive behavior. When appling the reduction peak (at 1.1 V) and the oxidation peak (at 2.1 V) to Equation 4, the b-values at different stage are calulated (Figure 5e). The high b-value at lithidation (0.73) and delithidation (0.81) process indicates the existence of pesudocapacitive behavior, which is positive for faster kinetics. The contribution ratio of pesudocapacitive behavior could be determined according to Equation 5. Normally, k_1 and k_2 is obtained by plotting $i/v^{1/2}$ versus $v^{1/2}$. At a given scan rate, the total capacitive contrition included two part: the one from diffusion-controlled fraction ($k_1v^{1/2}$), and the one from capacitor-like farction (k_2v). Figure 5f summarizes contribution ratios of the pseudocapacitve behavior at various scan rates. The reults demonstrate that pseudocapacitive charge-stroage amount contributes a high percentage of the whole capacity.

The unique structure of Co_3O_4 NP@NC@CNTs enables excellent cycling stability and ultrafast rate capability. Firstly, the small particle sizes of the Co_3O_4 NPs effectively shorten the ion diffusion distance and alleviate the problem of structural collapse during lithiation/delithiation processes. Secondly, the interconnected porous NC@CNTs host effectively accommodates the volume expansion of Co_3O_4 NPs and also enhances conductivity. Thirdly, the interconnected CNTs can strengthen the structural stability of the Co_3O_4 NP@NC units and enhance the conductive contact between different active particles, resulting in better utilization of the active materials.

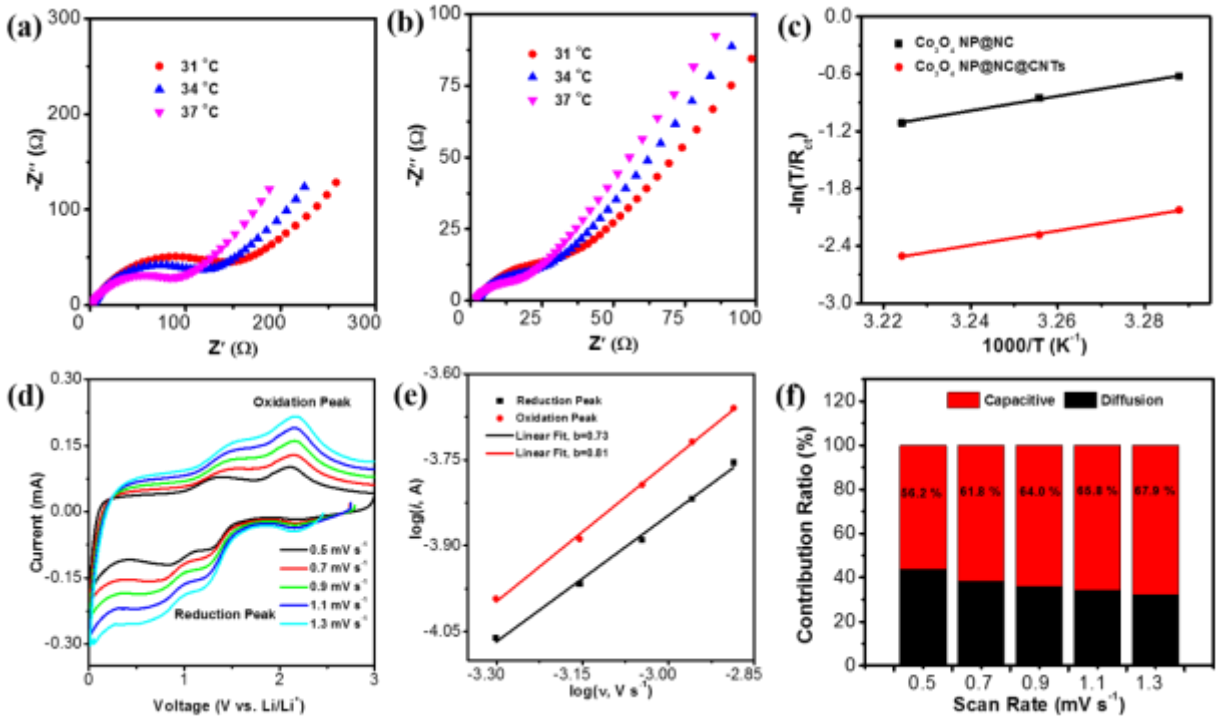

Figure 5. Nyquist plots of (a) Co_3O_4 NP@NC and (b) Co_3O_4 NP@NC@CNTs, at different temperatures, (c) the corresponding Arrhenius fitting plots of Co_3O_4 NP@NC and Co_3O_4 NP@NC@CNTs electrodes. (d) CV curves of Co_3O_4 NP@NC@CNTs at different scan rates from 0.5 to 1.3 mV s^{-1}, (e) the relationship between peak current and scan rate of Co_3O_4 NP@NC@CNTs at the reduction and oxidation process, (f) the normalize contribution ratio of pesudocapacitive behavior at different scan rate of Co_3O_4 NP@NC@CNTs.

4. Conclusion

In summary, a novel structure of Co_3O_4 NP@NC@CNTs, where Co_3O_4 NPs is covered by NC layers and further connected by CNTs, was synthesized by elaborately pyrolyze the ZIF-67 as precursor. The designed Co_3O_4 NP@NC@CNTs shows impressive potential for ultrafast LIBs in terms of high reversible capacity, long cycling stability, and very good capacity retention at high current density. To be specific, the high reversible capacity of 1017 mAh g^{-1} was delivered after

500 cycles at 1.0 A g^{-1}, and good capacity retention of 75% was observed after 5000 cycles at 15 A g^{-1}. The outstanding performance of Co_3O_4 NP@NC@CNTs is attributed to its unique structure, which can effectively accommodate the volume expansion of Co_3O_4 NPs and improve electron/ion transportation in and among the active particles. The electrochemical kinetics investigation confirmed a faster charge transfer rate and easier redox reactions. To the best of our knowledge, this is the best electrochemical performance among other reported Co-based electrodes. These results confirm the structural superiority of this Co_3O_4 NP@NC@CNTs electrode and would shed light the prospects for further designing other high performance LIB materials.

Associate Content

Supporting Information

The supporting information is available free of charge on the ASC Pubications website.

SEM images of ZIF-67, Co NP@NC, Co_3O_4 NP@NC@CNTs; XRD patterns of ZIF-67 and Co NP@NC; Raman curve for Co_3O_4 NP@NC; TGA curve of Co_3O_4 NP@NC; TEM images of Co_3O_4 NP @NC; N_2 isotherms of Co_3O_4 NP@NC@CNTs and Co_3O_4 NP@NC; Discharge/charge profiles of Co_3O_4 NP@NC@CNTs and Co_3O_4 NP@NC; Electrochemical comparison of the electrochemical performance reported in this work with other reports; Data for the Arrhenius fitting.

Author Information

Corresponding Authors

E-mail: wangc@jsnu.edu.cn (C. Wang)

E-mail: zhenguo.huang@uts.edu.au (Z. Huang)

E-mail: lei.zhang@griffith.edu.au (L. Zhang)

Acknowledgement

This work was supported by the National Natural Science Foundation of China (NSFC) (No. 51703087, 21805117), National Natural Science of the Higher Education Institutions of Jiangsu Province (No. 18KJB150015), Jiangsu Province Science Foundation for Youths (BK20180209), and the Priority Academic Program Development Fund of Jiangsu Higher Education Institutions.

REFERENCES

(1) Niu, S.; Wang, Z.; Zhou, T.; Yu, M.; Yu, M.; Qiu, J. A Polymetallic Metal-Organic Framework-Derived Strategy toward Synergistically Multidoped Metal Oxide Electrodes with Ultralong Cycle Life and High Volumetric Capacity. *Adv. Funct. Mater.* **2017**, *27*, 1605332.

(2) Xia, G.; Zhang, L.; Fang, F.; Sun, D.; Guo, Z.; Liu, H.; Yu, X. General Synthesis of Transition Metal Oxide Ultrafine Nanoparticles Embedded in Hierarchically Porous Carbon Nanofibers as Advanced Electrodes for Lithium Storage. *Adv. Funct. Mater.* **2016**, *26*, 6188-6196.

(3) Guo, W.; Sun, W.; Lv, L. P.; Kong, S.; Wang, Y. Microwave-Assisted Morphology Evolution of Fe-Based Metal-Organic Frameworks and Their Derived Fe_2O_3 Nanostructures for Li-Ion Storage. *ACS Nano* **2017**, *11*, 4198-4205.

(4) Wang, L.; Zhang, K.; Hu, Z.; Duan, W.; Cheng, F.; Chen, J. Porous CuO Nanowires as The Anode of Rechargeable Na-ion Batteries. *Nano Res.* **2013**, *7*, 199-208.

(5) Reddy, M. V.; Subba Rao, G. V.; Chowdari, B. V. Metal Oxides and Oxysalts as Anode

Materials for Li Ion Batteries. *Chem. Rev*. **2013**, *113*, 5364-5457.

(6) Wang, Y.; Wang, B. F.; Xiao, F.; Huang, Z. G.; Wang, Y. J.; Richardson, C.; Chen, Z. X.; Jiao, L. F.; Yuan, H. T. Facile Synthesis of Nanocage Co_3O_4 for Advanced Lithium-Ion Batteries. *J. Power Sources* **2015**, *298*, 203-208.

(7) Wang, Y.; Huang, Z. G.; Wang, Y. J. A New Approach to Synthesize MoO_2@C for High-Rate Lithium Ion Batteries. *J. Mater. Chem. A* **2015**, *3*, 21314-21320..

(8) Tian, W.; Hu, H.; Wang, Y.; Li, P.; Liu, J.; Liu, J.; Wang, X.; Xu, X.; Li, Z.; Zhao, Q.; Ning, H.; Wu, W.; Wu, M. Metal–Organic Frameworks Mediated Synthesis of One-Dimensional Molybdenum-Based/Carbon Composites for Enhanced Lithium Storage. *ACS Nano* **2018**, *12*, 1990-2000.

(9) Sun, J.; Lv, C.; Lv, F.; Chen, S.; Li, D.; Guo, Z.; Han, W.; Yang, D.; Guo, S. Tuning the Shell Number of Multishelled Metal Oxide Hollow Fibers for Optimized Lithium-Ion Storage. *ACS Nano* **2017,** *11*, 6186-6193.

(10) Su, Q.; Wang, S.; Xiao, Y.; Yao, L.; Du, G.; Ye, H.; Fang, Y. Lithiation Behavior of Individual Carbon-Coated Fe_3O_4 Nanowire Observed by in Situ TEM. *J. Phys. Chem. C* **2017**, *121*, 3295-3303.

(11) Yang, S. J.; Nam, S.; Kim, T.; Im, J. H.; Jung, H.; Kang, J. H.; Wi, S.; Park, B.; Park, C. R. Preparation and Exceptional Lithium Anodic Performance of Porous Carbon-Coated ZnO Quantum Dots Derived From a Metal-Organic Framework. *J. Am. Chem. Soc.* **2013**, *135*, 7394-7397.

(12) Bordiga, S.; Lamberti, C.; Ricchiardi, G.; Regli, L.; Bonino, F.; Damin, A.; Lillerud, K. P.; Bjorgen, M.; Zecchina, A. Electronic and Vibrational Properties of a MOF-5 Metal-Organic Framework: ZnO Quantum Dot Behaviour. *Chem. Commun*. **2004**, *12*, 2300-2301.

(13) Salunkhe, R. R.; Kaneti, Y. V.; Yamauchi, Y. Metal–Organic Framework-Derived Nanoporous Metal Oxides toward Supercapacitor Applications: Progress and Prospects. *ACS Nano* **2017**, *11*, 5293-5308.

(14) Zhao, Y.; Song, Z.; Li, X.; Sun, Q.; Cheng, N.; Lawes, S.; Sun, X. Metal Organic Frameworks for Energy Storage and Conversion. *Energy Storage Mater*. **2016**, *2*, 35-62.

(15) Xia, W.; Mahmood, A.; Zou, R.; Xu, Q. Metal-Organic Frameworks and Their Derived Nanostructures for Electrochemical Energy Storage and Conversion. *Energ. Environ. Sci*. **2015**, *8*, 1837-1866.

(16) Wang, Y.; Wang, C. Y.; Wang, Y. J.; Liu, H. K.; Huang, Z. G. Superior Sodium-Ion Storage Performance of Co_3O_4@Nitrogen-Doped Carbon: Derived From a Metal-Organic Framework. *J. Mater. Chem. A* **2016**, *4*, 5428-5435.

(17) Jiang, T.; Bu, F.; Feng, X.; Shakir, I.; Hao, G.; Xu, Y. Porous Fe_2O_3 Nanoframeworks Encapsulated within Three-Dimensional Graphene as High-Performance Flexible Anode for Lithium-Ion Battery. *ACS Nano* **2017**, *11*, 5140-5147.

(18) Sui, Z.-Y.; Zhang, P.-Y.; Xu, M.-Y.; Liu, Y.-W.; Wei, Z.-X.; Han, B.-H. Metal–Organic Framework-Derived Metal Oxide Embedded in Nitrogen-Doped Graphene Network for High-Performance Lithium-Ion Batteries. *ACS Appl. Mater. Inter*. **2017**, *9*, 43171-43178..

(19) Su, D. W.; Cortie, M.; Wang, G. X. Fabrication of N-doped Graphene-Carbon Nanotube Hybrids from Prussian Blue for Lithium-Sulfur Batteries. *Adv. Energy Mater.* **2017**, *7*, 5768-5777.

(20) Zhang, H.; Wang, Y.; Zhao, W.; Zou, M.; Chen, Y.; Yang, L.; Xu, L.; Wu, H.; Cao, A. MOF-Derived ZnO Nanoparticles Covered by N-Doped Carbon Layers and Hybridized on Carbon Nanotubes for Lithium-Ion Battery Anodes, *ACS Appl. Mater. Inter.* **2017**, *9*, 37813-37822.

(21) Lou, P.; Cui, Z.; Jia, Z.; Sun, J.; Tan, Y.; Guo, X. Monodispersed Carbon-Coated Cubic NiP_2 Nanoparticles Anchored on Carbon Nanotubes as Ultra-Long-Life Anodes for Reversible Lithium Storage. *ACS Nano* **2017**, *11*, 3705-3715.

(22) Chen, T.; Cheng, B.; Zhu, G.; Chen, R.; Hu, Y.; Ma, L.; Lv, H.; Wang, Y.; Liang, J.; Tie, Z.; Jin, Z.; Liu, J. Highly Efficient Retention of Polysulfides in "Sea Urchin"-Like Carbon Nanotube/Nanopolyhedra Superstructures as Cathode Material for Ultralong-Life Lithium–Sulfur Batteries. *Nano Letters* **2016**, *17*, 437-444.

(23) Dou, Y. H.; Xu, J. T.; Ruan, B. Y.; Liu, Q. N.; Pan, Y. D.; Sun, Z. Q.; Dou, S. X. Atomic Layer-by-Layer Co_3O_4/Graphene Composite for High Performance Lithium-Ion Batteries. *Adv. Energy Mater*. **2016**, *6*, 5768-5777.

(24) Zhang, C.; Fu, L.; Liu, N.; Liu, M.; Wang, Y.; Liu, Z. Synthesis of Nitrogen-Doped Graphene Using Embedded Carbon and Nitrogen Sources. *Adv. Mater*. **2011**, *23*, 1020-1024.

(25) Wang, H. B.; Maiyalagan, T.; Wang, X. Review on Recent Progress in Nitrogen-Doped Graphene: Synthesis, Characterization, and Its Potential Applications. *ACS Catal*. **2012**, *2*, 781-794.

(26) Wei, J.; Hu, Y.; Liang, Y.; Kong, B.; Zhang, J.; Song, J.; Bao, Q.; Simon, G. P.; Jiang, S. P.; Wang, H. Nitrogen-Doped Nanoporous Carbon/Graphene Nano-Sandwiches: Synthesis and Application for Efficient Oxygen Reduction. *Adv. Funct. Mater*. **2015**, *25*, 5768-5777.

(27) Yang, L.; Zeng, X.; Wang, W.; Cao, D. Recent Progress in MOF-Derived, Heteroatom-Doped Porous Carbons as Highly Efficient Electrocatalysts for Oxygen Reduction Reaction in Fuel Cells. *Adv. Funct. Mater*. **2017**, *12*, 1704537.

(28) Zheng, F.; Yang, Y.; Chen, Q. High Lithium Anodic Performance of Highly Nitrogen-Doped Porous Carbon Prepared from A Metal-Organic Framework. *Nat. Commun.* **2014**, *5*, 5261.

(29) Liu, Y. C.; Zhang, N.; Yu, C. M.; Jiao, L. F.; Chen, J. $MnFe_2O_4$@C Nanofibers as High-Performance Anode for Sodium-Ion Batteries. *Nano Letters* **2016**, *16*, 3321-3328.

(30) Li, H. H.; Li, Z. Y.; Wu, X. L.; Zhang, L. L.; Fan, C. Y.; Wang, H. F.; Li, X. Y.; Wang, K.; Sun, H. Z.; Zhang, J. P. Shale-like Co_3O_4 for High Performance Lithium/Sodium Ion Batteries. *J. Mater. Chem. A* **2016**, *4*, 8242-8248.

(31) Xu, G.-L.; Li, J.-T.; Huang, L.; Lin, W.; Sun, S.-G. Synthesis of Co_3O_4 Nano-Octahedra Enclosed by {111} Facets and Their Excellent Lithium Storage Properties as Anode Material of Lithium Ion Batteries. *Nano Energy* **2013**, *2*, 394-402.

(32) Kang, Y.-M.; Song, M.-S.; Kim, J.-H.; Kim, H.-S.; Park, M.-S.; Lee, J.-Y.; Liu, H. K.; Dou, S. X. A Study on ohe Charge–Discharge Mechanism of Co_3O_4 as an Anode for the Li Ion Secondary Battery. *Electrochim. Acta* **2005**, *50*, 3667-3673.

(33) Wang, B.; Lu, X.-Y.; Wong, K. Y.; Tang, Y. Facile Solvothermal Synthesis and Superior Lithium Storage Capability of Co_3O_4 Nanoflowers with Multi-Scale Dimensions. *Mater. Chem. Front*. **2017**, *1*, 468-476.

(34)Gu, D.; Li, W.; Wang, F.; Bongard, H.; Spliethoff, B.; Schmidt, W.; Weidenthaler, C.; Xia, Y.; Zhao, D.; Schüth, F. Controllable Synthesis of Mesoporous Peapod-like Co_3O_4@Carbon Nanotube Arrays for High-Performance Lithium-Ion Batteries. *Angew. Chem. Int. Ed*. **2015**, *54*, 7060-7064.

(35) Huang, G.; Zhang, F.; Du, X.; Qin, Y.; Yin, D.; Wang, L. Metal Organic Frameworks Route to in Situ Insertion of Multiwalled Carbon Nanotubes in Co_3O_4 Polyhedra as Anode Materials for Lithium-Ion Batteries. *ACS Nano* **2015**, *9*, 1592-1599.

(36) Yan, C.; Zhu, Y.; Li, Y.; Fang, Z.; Peng, L.; Zhou, X.; Chen, G.; Yu, G. Local Built-In Electric Field Enabled in Carbon-Doped Co_3O_4 Nanocrystals for Superior Lithium-Ion Storage. *Adv.*

Funct. Mater. **2018**, *28*, 1705951.

(37) Yang, Y.; Huang, J.; Zeng, J.; Xiong, J.; Zhao, J. Direct Electrophoretic Deposition of Binder-Free Co_3O_4/Graphene Sandwich-Like Hybrid Electrode as Remarkable Lithium Ion Battery Anode. *ACS Appl. Mater. Inter*. **2017**, *9*, 32801-32811.

(38) Cao, K.; Jiao, L.; Liu, Y.; Liu, H.; Wang, Y.; Yuan, H. Ultra-High Capacity Lithium-Ion Batteries with Hierarchical CoO Nanowire Clusters as Binder Free Electrodes. *Adv. Funct. Mater*. **2015**, *25*, 1082-1089

The Table of Contents